

Electron capture cross sections and nuclear partition functions for fp -shell nuclei

Jameel-Un Nabi* and Muhammad Riaz
GIK Institute of Engineering Sciences and Technology, Topi 23640,
Khyber Pakhtunkhwa, Pakistan.
(Dated: March 11, 2025)

We present calculation of electron capture cross sections (ECC), in the limit of zero momentum transfer, using the pn-QRPA model in stellar matter. Towards this aim we make use of our recently introduced recipe for estimation of nuclear partition functions. For low momentum transfer ($q \rightarrow 0$), the nuclear matrix elements of the $\sum \sigma\tau^+$ operator provide the leading contribution to the total cross section which we estimate using the pn-QRPA model in a multi-shell single-particle space with a schematic interaction. Key fp -shell nuclei (odd A , even-even and odd-odd) bearing astrophysical importance were selected for the calculation of ECC in stellar environment. These fp -shell nuclei play crucial role in pre-supernova evolution of massive stars and core collapse. We further present microscopic calculation of ground and excited states Gamow-Teller strength distributions and stellar electron capture rates on these suite of nuclei. We used two different sets of empirically determined pairing gaps to calculate the ECC and electron capture rates. Results are compared with experimental data and previous computations. Our calculated ECC are systematically smaller at low electron incident energies as compared to the shell-model results.

PACS numbers: 21.10.Ma; 21.60.Jz; 23.40.-s; 26.30.Jk; 26.50.+x

I. INTRODUCTION

The explosive scenario in which massive stars end their lives is a well known phenomenon called supernova. Evolution of massive stars and the associated supernova explosion are intricately connected to the synthesis of elements. It has been stressed with the passage of time that calculations of stellar nucleosynthesis, neutrino-induced reactions and nuclear aspects of supernova collapse & simulation be based on *microscopic* global predictions for the nuclear ingredients rather than on simplified semi-empirical approaches. Determination of mass of the stellar core, commencement of gravitational collapse of the core of a massive star, thereby triggering a supernova explosion, and fate of the resulting shock wave, are few astrophysical events where electron capture rates play a crucial role.

The electron capture cross section on iron group nuclei as well as capture of electrons on free protons play a significant role during the pre-collapse phases. It is a well established fact that, for low stellar temperatures (3.5–9.3 GK) and densities ($\sim 10^{10} \text{ gcm}^{-3}$), electron capture rates are sensitive to the associated Gamow-Teller (GT) strength distribution (as the electron chemical potential is at par with the nuclear Q value). Under such conditions electron capture mainly occurs on heavy nuclei with $A \sim 60$. As the stellar core stiffens to higher densities and temperatures sore further, the electron chemical potential exceeds the Q value, and in this phase, electron capture rates are largely dictated by the total GT strength and its centroid energy. Under these conditions electron capture occurs on heavier nuclei $A \geq 60$. For even larger values of electron chemi-

cal potential ($\geq 20 \text{ MeV}$) corresponding to stellar densities $\geq 10^{11} \text{ gcm}^{-3}$, forbidden transitions become significant and should no longer be neglected. For further details and references see [1]. It is therefore desirable to have a microscopic calculation of GT strength distributions, preferably for dozens of nuclei, for a reliable prediction of electron capture rates on sd -, fp - and fpg -shell nuclei. Theoretical estimations for GT distributions fall generally into three genre: simple independent-particle models (e.g. Ref. [2]); full-scale interacting shell-model; and, in between, the random-phase approximation (RPA) and quasi-particle random-phase approximation (QRPA). Independent-particle models usually underestimate the total GT strength. One reason for this is the insufficient fragmentation of the Fermi surface. At the same time these models tend to place the centroid of the GT strength too high for even-even parent nuclei and too low on odd- A and odd-odd parents [3]. On the other end, full interacting shell-model calculations are computationally taxing. In these models one may use the Lanczos algorithm to generate the GT strength distribution. However, for medium-mass nuclei, one still needs to choose from among a number of competing semi-realistic/semi-empirical interactions. RPA/QRPA models may be taken as decent approximations to a full shell-model calculation and are computationally much less taxing.

There is yet another challenge for the weak-interaction rate calculations and associated nuclear models. Stellar rates take place at temperatures of the order of a few hundred Kelvin's to a few GK 's. At such high temperatures the GT transitions are possible not only from the usual ground state, but also from parent excited states. This is precisely where most of the nuclear models compromise to approximations, e.g. Brink-Axel hypothesis [4] and back resonances. Brink-Axel hypothesis states that GT strength distribution on excited states is *iden-*

* jameel@giki.edu.pk

tical to that from ground state, shifted *only* by the excitation energy of the state. GT back resonances are the states reached by the GT transitions in the electron capture direction built on ground and excited states. The independent-particle shell model calculation (e.g. [2]), spectral distribution theory (e.g. [5]) and shell-model diagonalization approach (e.g. [3]) are few of the models that used such approximations in calculation of weak-rates. It is to be noted that shell model diagonalization approach estimates stellar weak rates, in a microscopic fashion, only up to first few MeV of parent excitation energy. For higher parent excitation energies they revert back to the Brink-Axel hypothesis. Later Nabi and Klapdor-Kleingrothaus [6–8] showed that Brink-Axel hypothesis and back resonances are not a good approximation for use in stellar rates. Dzhioev and collaborators [9] introduced the thermofield dynamics (TFD) formalism for calculation of stellar rates that took into consideration the weak-interaction response at finite temperatures. The authors demonstrated that thermal effects shifted the GT centroid to lower excitation energy. The TFD formalism also avoided the use of Brink-Axel hypothesis. On a microscopic level handling of GT strength distributions and associated weak-interaction rates under stellar conditions can be tackled using two different schemes. One (and the preferred) method is a state-by-state microscopic evaluation of the rate summing over Boltzmann-weighted, individually determined GT strengths for the various states (e.g. stellar weak rates calculation using the pn-QRPA model [6–8]). The second is based on an equilibrium statistical formulation of many-body problem (normally referred to as shell-model Monte Carlo (SMMC) method) (e.g. [10]). The SMMC calculation found that the GT centroid shifted to lower excitation energies and resulted in bigger widths (primarily due to appearance of low-lying states) as temperature increases. Both the pn-QRPA and SMMC calculations did not support the Brink-Axel hypothesis. Despite some success, path-integral methods are limited to interactions not plagued with the "sign problem". They are computationally very demanding (i.e., require supercomputer time). At low temperatures the SMMC method has few restrictions in its applicability to odd-A and odd-odd nuclei. The pn-QRPA model can be used for any arbitrarily heavy system of nucleons. The thermodynamic conditions spanned over several $100ms$ time interval post bounce in core-collapse supernova simulation have been analyzed [11], where the density range spanned about 10 orders of magnitude ($10^5 - 10^{15} gcm^{-3}$), the temperature around two orders (1 - 589 GK) and the lepton fraction more than an order of magnitude (0.01 - 0.5). The large variety of nuclear matter properties lead to distinct outcomes in supernova simulations. The rate of change of lepton-to-baryon fraction (Y_e) depends both on mass fractions and weak-interaction rates of the nuclei.

Accurate and reliable estimates of nuclear partition functions (NPFs) are a prerequisite for the determination of the electron capture cross sections. NPFs also

play key role in other astrophysical processes, e.g. determining equation of state during gravitational collapse [2], mass fractions determination in the presupernova matter [12] and abundance calculations during silicon burning phases of stars [13]. Authors in Ref. [14] performed computation of NPFs and reaction rates for nuclei with $10 \leq Z \leq 83$ using the Hauser-Feshbach formalism. The chosen temperature range was $0.01 \leq T \leq 10 GK$. Two different mass models, namely the finite range droplet model (FRDM) [15] and an extended Thomas-Fermi approach with Strutinski integral (ETFSI) [16], were employed for their calculation of NPFs. Later Rauscher [17] extended his estimation of NPF to extreme conditions ($12 GK \leq T \leq 275 GK$ with $9 \leq Z \leq 85$) applying high-temperature corrections. The authors followed a statistical approach throughout the nuclear chart. They did not incorporate experimental level density parameters and noted that this may lead to slightly larger deviations from experiment. Low-lying nuclear levels need to be treated as discrete and calculated NPFs can change substantially by performing a summation over these discrete levels [18]. The calculated NPF poses one of the biggest uncertainties in the estimation of mass fractions for nuclei in presupernova cores. The calculated NPFs displayed a variation of up to 50% when discrete energy levels were summed as against those assuming a level density function and performing integration over continuous states [18]. Inspired by this recipe, Nabi and collaborators [19, 20] recently calculated discrete energy levels in 700+ nuclei, up to excitation energy of 10 MeV , supplemented by experimental data whenever available, and assumed a simple level density function (for performing integration beyond 10 MeV) to come up with a reliable estimation of NPFs. The same recipe for estimation of NPFs was used in this work. We calculate GT strength distributions using the pn-QRPA model and NPFs in this paper. These functions were later used to estimate the electron capture cross section on odd-A (^{45}Sc , ^{51}V , ^{55}Fe , ^{59}Co), even-even ($^{54,58}Fe$) and odd-odd ($^{56,58}Mn$) nuclei. All selected nuclei bear astrophysical significance (belonging to the iron-regime group and advocated to play significant role in the presupernova evolution of massive stars). We also present computation of associated electron capture rates for few nuclei in this paper.

In the next section we introduce the necessary formalism adopted in our calculation. Section III presents our estimation of GT distribution functions, NPFs, ECC and electron capture rates. We further compare our computation with previous calculations in this section. Section IV finally states our conclusions.

II. THEORETICAL FRAME WORK FOR CALCULATED NUCLEAR PROPERTIES

A. The pn-QRPA formalism

The single-particle states were calculated using a deformed Nilsson potential [21]. The proton-proton and neutron-neutron pairing correlations were explicitly taken into account in the Bardeen-Cooper-Schiff (BCS) theory. We employed the BCS calculation for neutron and proton systems independently. Ground state correlations, two-particle and two-hole mixing states were included in the pn-QRPA model. The ground states of parent nucleus $|i\rangle$ were computed using the BCS equations. The excited states of daughter nuclei $|f\rangle$ and connecting GT transitions were calculated using the pn-QRPA equations [22]. The Hamiltonian was taken as

$$H^{pn-QRPA} = H^{sp} + V^{pair} + V_{GT}^{ph} + V_{GT}^{pp}, \quad (1)$$

where H^{sp} is the single-particle Hamiltonian, V^{pair} is the pairing force, V_{GT}^{ph} is the particle-hole (ph) GT force and V_{GT}^{pp} is the particle-particle (pp) GT force. The proton-neutron residual interactions occurred as particle-hole and particle-particle interaction in our model. Nilsson potential parameters were adopted from Ref. [23], Q-values were taken from the recent mass compilation of Audi et al. [24] and $\hbar\omega = 41/A^{1/3}$ in units of MeV was considered for Nilsson oscillator constant (similar for neutrons and protons). The BCS calculation provided occupation amplitudes and quasiparticle energies. It is to be noted that the pairing gaps (Δ) were not calculated using the BCS theory and were determined empirically in our calculation. The pairing gaps (in units of MeV) were calculated using two different schemes. In the first method we chose the pairing gaps according to the global systematics [25]

$$\Delta_n = \Delta_p = 12/\sqrt{A}, \quad (2)$$

We called these pairing gap values as Scheme-I in this paper.

The pairing gaps can also be determined from the empirical masses of a sequence of isotopes or isotones. This 3-point formula is given by [25]

$$\Delta_n = \frac{1}{4}(-1)^{A-Z+1}[S_n(A-1, Z) - 2S_n(A, Z) + S_n(A+1, Z)] \quad (3)$$

$$\Delta_p = \frac{1}{4}(-1)^{Z+1}[S_p(A+1, Z+1) - 2S_p(A, Z) + S_p(A-1, Z-1)] \quad (4)$$

The 3-point formula was referred to as Scheme-II in this paper. Table 1 shows the calculated values of pairing gaps using the two schemes. We investigated the effect of pairing gaps on the calculated electron capture rates and cross sections which we discuss in the next section.

Mean-field calculations can determine the deformations of nuclei (e.g., by calculating potential energy surfaces). We on the other hand determined the nuclear quadruple deformation parameter (β_2) using the formula

$$\beta_2 = \frac{125(Q_2)}{1.44(A)^{2/3}(Z)}, \quad (5)$$

where Q_2 denotes the electric quadrupole moment taken from Ref. [26]. The calculation of Δ and β_2 was not performed in a self-consistent way in our model. For further details of the pn-QRPA formalism and selection of model parameters we refer to [27].

B. The GT strength distributions

In the pn-QRPA model the charge-changing transitions are described by phonon creation operators defined by

$$A_\omega^+(\mu) = \sum_{pn} (X_\omega^{pn}(\mu)a_p^+a_n^+ - Y_\omega^{pn}(\mu)a_n a_{\bar{p}}). \quad (6)$$

The summation was taken over all the $p-n$ pairs having $\mu = (m_p - m_n) = 0, \pm 1$, where $m_n(m_p)$ denotes the third component of angular momentum for neutron (proton). The $a_{n(p)}^+$ are the creation operator of a quasi-particle state of neutron (proton). The \bar{p} (\bar{n}) represents the time reversed state of p (n). The excitation energy (ω) and corresponding amplitudes (X_ω, Y_ω) of phonon operator were obtained by solving the usual RPA equation. The ground level of our model with respect to the QRPA phonon was taken as the vacuum, $A_\omega(\mu)|QRPA\rangle = 0$. Detailed solution of RPA matrix equation may be seen from Refs. [28, 29].

Construction of parent and daughter excited states in our model may be seen from appendix A.

C. Nuclear partition functions

A novel recipe for the calculation of nuclear partition functions (NPFs) was recently introduced [19, 20]. The two key features of this recipe were (i) treatment of low-lying nuclear states (up to 10 MeV) as discrete ones, and (ii) incorporation of experimental data (energy levels and J^π values) wherever possible. The authors in Ref. [18] concluded that treatment of low-lying states as discrete can lead to substantial changes in the calculated NPF. These were computed as

$$G(A, Z, T) = \sum_{i=0}^{i_m} (2J_i + 1) \exp[-E_i/kT] + \int_{E^{i_m}}^{E^{max}} \sum_{J_i, \pi_i} (2J_i + 1) \exp(-\epsilon/kT) \rho_{nucl}(\epsilon, J_i, \pi_i) d\epsilon, \quad (7)$$

with i_m being the label of last included experimentally known and/or theoretically calculated parent energy state. In Eq. (7), ρ_{nucl} is the nuclear level density and other symbols have their usual meanings. Above the last discrete state an integration was performed over the nuclear level density. We used the Bardeen-Cooper-Schriffer (BCS) equations to construct the discrete energy levels, up to 10 MeV, for all nuclide under consideration. For higher excited states we assumed a uniform Fermi gas and estimated the level density (using saddle point approximation yields and some additional simplifications) as [30]

$$\rho_{nucl}(\epsilon, J_i, \pi_i) \approx \rho_{nucl}(A, E) = \frac{\exp(2\sqrt{aE})}{4\sqrt{3}E}, \quad (8)$$

where $a = \frac{\pi^2 g}{6}$ and the density of single particle states for a nucleus having A fermions is $g = \frac{3A}{2E_F}$ where E_F is the Fermi energy. For further details on estimation of NPFs we refer to [19, 20].

D. Electron capture cross sections

The β -decay and electron capture are the competitive processes in opposite directions, controlling the lepton-to-baryon fraction of stellar matter during presupernova phases of massive stars and given, respectively, by

$$(Z, N) \longrightarrow (Z + 1, N - 1) + e^- + \bar{\nu}_e, \quad (9)$$

$$e^- + (Z, N) \longrightarrow \nu_e + (Z - 1, N + 1). \quad (10)$$

The nucleus (Z, N) captures electron of incident energy (w) and interacts weakly as shown in Eq. (10). The electron energy is distributed into two parts: a part of it is absorbed by daughter nucleus to change from initial E_i to final state E_f and the remaining energy is carried out by emitted neutrino. The nuclear reaction cross section calculation for the electron capture is governed by the weak-interaction Hamiltonian

$$\hat{H}_\omega = \frac{G}{\sqrt{2}} j_\mu^{lept} \hat{J}^\mu, \quad (11)$$

where $G = G_F \cos \theta_c$, G_F is the Fermi coupling constant and θ_c is Cabibbo angle. The j_μ^{lept} and \hat{J}^μ are the leptonic and hadronic currents, respectively, given as

$$j_\mu^{lep} = \bar{\psi}_e(x) \gamma_\mu (1 - \gamma_5) \psi_\nu(x) \quad (12)$$

$$\hat{J}^\mu = \bar{\psi}_p(x) \gamma_\mu (1 - c_A \gamma_5) \psi_n(x), \quad (13)$$

where ψ are the spinor operators. In leptonic current the axial vector coupling and vector coupling are of the same strength but in hadronic current the axial component contains a factor of c_A that is not equal to one.

Our main task was to estimate electron capture cross sections (ECC) of nuclear reaction based on the calculation of nuclear transition matrix elements between the initial $|i\rangle$ and final $|f\rangle$ nuclear states

$$\langle f | |\hat{H}_\omega| | i \rangle = \frac{G}{\sqrt{2}} l^\mu \int d^3x e^{-i\mathbf{q}\cdot\mathbf{x}} \langle f | \hat{J}_\mu | i \rangle, \quad (14)$$

where \mathbf{q} shows the three-momentum transfer and $l^\mu e^{-i\mathbf{q}\cdot\mathbf{x}}$ are the leptonic matrix element used for calculation of transition matrix element [31, 32]. The nuclear transition matrix elements can be computed with the help of Donnelly-Walecka multipolar decomposition that leads to charge, longitudinal, transverse electric and transverse magnetic multipole operators [32]. We, however, used the approximation $q \rightarrow 0$ assuming low momentum transfer. Using this limiting case, the transitions of the GT_+ ($= \sum \tau^+ \sigma$) operator provide the leading contribution to the total ECC [33].

The total stellar ECC on the target nucleus of mass number A and charge number Z , as a function of incident electron energy (w) and temperature (T) , is given by

$$\begin{aligned} \sigma(w, T) = & \frac{G_F^2 \cos^2 \theta_c}{2\pi} \sum_i F(Z, w) \frac{(2J_i + 1) \exp(-E_i/kT)}{G(A, Z, T)} \\ & \times \sum_{J, f} (w - Q + E_i - E_f)^2 \frac{|\langle i | \hat{O}_J | f \rangle|^2}{(2J_i + 1)}, \end{aligned} \quad (15)$$

where $F(Z, w)$ is the Fermi function and accounts for the distortion of the electron's wave function due to the Coulomb field of the nucleus and finite size of the nucleus. The Fermi function was calculated using the prescription of Ref. [34]. The $G(A, Z, T)$ are the NPFs and their computation was discussed in the previous section. The J_i 's are the angular momenta of parent states. The \hat{O}_J operator, appearing in the nuclear matrix elements of Eq. (15), reduces to the GT_+ operator (which changes a proton into a neutron) for low three-momentum transfer. We quenched the GT strength by a constant factor of 0.6 [35].

E. Electron capture rates

The electron capture (EC) rate of a transition from the i^{th} state of the parent to the f^{th} state of the daughter nucleus is given by

$$\begin{aligned} \lambda_{if}^{EC} = & \left[\frac{\ln 2}{D} \right] [f_{if}(T, \rho, E_F)] \\ & \left[B(F)_{if} + \left(g_A/g_V \right)_{eff}^2 B(GT)_{if} \right]. \end{aligned} \quad (16)$$

The value of constant D was taken to be 6143s [36]. B'_{if} 's are the sum of reduced transition probabilities of

the Fermi and Gamow-Teller transitions given by

$$B(F)_{if} = \frac{1}{2J_i + 1} \langle f \parallel \sum_k \tau_k^+ \parallel i \rangle^2 \quad (17)$$

$$B(GT)_{if} = \frac{1}{2J_i + 1} \langle f \parallel \sum_k \tau_k^+ \vec{\sigma}^k \parallel i \rangle^2. \quad (18)$$

The f_{if} is the phase space integral over total energy and for electron capture it is given by (using natural units $\hbar = c = m_e = 1$):

$$f_{if} = \int_{w_l}^{\infty} w \sqrt{w^2 - 1} (w_m + w)^2 F(Z, w) \Lambda_- dw. \quad (19)$$

In the above equation w is the incident electron energy, w_l is the total capture threshold energy (rest+kinetic) for electron capture, w_m is the total decay energy

$$w_m = m_p - m_d + E_i - E_f, \quad (20)$$

where m_p and E_i are mass and excitation energies of the parent nucleus, and m_d and E_f of the daughter nucleus, respectively. $F(Z, w)$ are the Fermi functions and Λ_- is the Fermi-Dirac distribution function for electrons

$$\Lambda_- = \left[\exp\left(\frac{E - E_F}{kT}\right) + 1 \right]^{-1}. \quad (21)$$

Here $E = (w - 1)$ is the kinetic energy of the electrons, E_F is the Fermi energy of the electrons and k is the Boltzmann constant.

The number density of electrons associated with protons and nuclei is $\rho Y_e N_A$ (ρ is the baryon density and N_A is Avogadro's number) where,

$$\rho Y_e = \frac{1}{\pi^2 N_A} \left(\frac{m_e c}{\hbar}\right)^3 \int_0^{\infty} (\Lambda_- - \Lambda_+) p^2 dp, \quad (22)$$

here $p = (w^2 - 1)^{1/2}$ is the electron momentum and Eq. (22) has the units of $mol \text{ cm}^{-3}$. Λ_+ is the Fermi-Dirac distribution function for positrons,

$$\Lambda_+ = \left[\exp\left(\frac{E + 2 + E_F}{kT}\right) + 1 \right]^{-1}. \quad (23)$$

We note that Fermi-Dirac distribution functions were used in Eqs. (21) and (23) as the electrons were assumed to be in continuum state in stellar matter. Eq. (22) was used for an iterative calculation of Fermi energies for selected values of Y_e and T . There is a finite probability of occupation of parent excited states in the stellar environment as a result of the high temperature in the interior of massive stars. EC rates then also have a finite contribution from these excited states. The total electron capture rate per unit time per nucleus was then computed using

$$\lambda^{EC} = \sum_{if} P_i \lambda_{if}^{EC}. \quad (24)$$

The summation over all initial and final states was carried out until satisfactory convergence in the EC rate was achieved in our calculation. In Eq. (24) P_i is the probability of occupation of parent excited states and follows the normal Boltzmann distribution.

III. RESULTS AND DISCUSSION

We start the proceedings by presenting the calculated GT strength distributions using the pn-QRPA model. The pn-QRPA model estimates ground and excited states GT strength distributions in a *microscopic* fashion. In other words the Brink-Axel hypothesis was not assumed in the calculation of excited states GT distributions. Figs. 1-2 show the computed GT strength distributions for the ground and first two excited states of ^{45}Sc , ^{56}Mn , ^{58}Fe and ^{59}Co , respectively. The abscissa shows the excitation energy (in units of MeV) in daughter nuclei. As mentioned earlier an overall quenching factor of 0.6 [35] was adopted in the estimation of GT strength for all nuclei. Calculated GT transitions of magnitude less than 10^{-4} are not shown in these figures. In Fig. 1, for ground states, the experimental data is shown by squares. The pn-QRPA transitions are shown by circles. The top-left panel of Fig. 1 shows a prominent peak from ground state of parent (^{45}Sc) of magnitude 1.1 at 6.2 MeV in ^{45}Ca . The peak strength shifts to a lower excitation energy of 4.9 (3.4) MeV for the first (second) excited state. The right panels of Fig. 1 show that the total GT strength from ground state of ^{59}Co is much bigger than those from excited states. For the case of ^{56}Mn (see left panels of Fig. 2) the low-lying GT peaks disappear for the second excited state. Similarly right panels of Fig. 2 show that the ground-state GT strength distribution for ^{58}Fe is well populated, not to be seen for the first and second excited states. The GT distributions are also different for high-lying excited states. Complete set of GT strength distribution functions for higher excited states may be requested from the authors. Fig. 1 and Fig. 2 clearly show that Brink-Axel hypothesis is not a good approximation to be used for the calculation of stellar ECC and EC rates.

Tables II – III show our computed NPFs as a function of stellar temperature (GK) for few fp -shell nuclei of astrophysical importance. We further compare our results with the statistical model calculation of Refs. [14, 17]. The finite range droplet model (FRDM) [15] was used as one of the input mass models to calculate the NPFs by Ref. [14]. It is to be noted that the estimations of NPFs by Refs. [14, 17] were normalized to the ground-state spin multiplicity whereas our NPFs include the ground-state spin multiplicity factor. We compare our estimated NPFs with those calculated by Ref. [14] up to a temperature of 10 GK . At 30 GK we compare our NPFs with the computation of Ref. [17] where high-temperature corrections were incorporated by Rauscher. At low temperatures ($\geq 0.5 GK$) we do notice significant differences in the two

calculations, specially for nuclei where angular momentum of ground-state differs significantly from zero. We incorporated experimental energy levels (along with their spins) in calculation of our NPFs missing in the statistical model. The NPFs computed by Rauscher are orders of magnitude bigger at 30 *GK* and higher temperatures. This we attribute to incorporation of high-temperature correction effects in Rauscher's computation which was missing in our estimation. This we take as a drawback in our calculation.

Matrix elements of the $\sum \sigma\tau^+$ operator and NPFs are two key microscopic ingredients in the calculation of stellar ECC. After displaying our results for the estimation of GT strength distributions and NPFs, we now present our calculation of ECC for key *fp*-shell nuclei in stellar environment. We calculated our ECC for stellar temperatures (5.8 - 17.4 *GK*). At these temperatures the GT transitions are unblocked as the residual interaction becomes sufficiently strong. The allowed GT₊ transitions are Pauli blocked at low temperature due to closed neutron *f* sub-shell. As the temperature increases unblocking of closed shells take place. Similarly GT₊ transition can undergo by thermally excited protons. The important range of the incident electron energy (*w*) is up to 30 *MeV* [1]. Accordingly we present our calculated ECC in Figs. 3 - 6 up to *w* = 30 *MeV*.

Left panels of Fig. 3 shows our estimated ECC for odd-A nucleus ⁴⁵Sc as a function of incident electron energy. We calculated the ECC at stellar temperatures of 5.8, 11.6 and 17.4 *GK*, respectively. The minimum electron energy to initiate the electron capture process is given by Eq. (32). However at finite temperatures, this threshold is further lowered by the internal excitation energy. The ECC increases drastically within the first few *MeV*'s of *w* above threshold. This effect maybe traced to the behavior of calculated GT distribution. The bottom-left panel of Fig. 3 reproduces the shell model Monte Carlo computation of ECC at a temperature of 5.8 *GK* [10]. At low *w* (~ 2.5 *MeV*) our calculated ECC is around three orders of magnitude smaller. At low incident electron energies the capture process is sensitive to the details of GT strength distribution. The GT strength distributions of ground and first two excited states of ⁴⁵Sc were presented earlier in Fig. 1. The SMMC model predicts marginally larger cross sections at low *w*. This result is expected due to the strong configuration mixing in SMMC calculation (also see Ref. [37] for further discussion). For electron energy $w \geq 10$ *MeV* the estimated cross sections display a more gradual increase. At high incident electron energy of 29.5 *MeV* the reported ECC is roughly factor two larger. It is to be noted that at low *w*, the calculated ECC are very small numbers and can change by orders of magnitude with a rather small change in the computed GT strength distributions and NPFs. Moreover these numbers are much smaller than those at $w \geq 10$ *MeV* and consequently the total electron capture rates calculated by the two models may not be significantly different in the low-energy interval. It may however depend

strongly on prevailing stellar density and temperature values (see related discussion in Refs. [10, 32]). With increasing *w* the ECC continues to rise modestly (because of the $(w - Q + E_i - E_f)^2$ factor in Eq. (27)). In the SMMC estimation only the $0\hbar\omega$ GT transition strength was considered, rather than the total strength in the 1⁺ channel. As the temperature increases from 5.8 *GK* to 11.6 *GK*, we witness a notable increase up to an order of magnitude in the calculated ECC and corresponds to an appreciable thermal unblocking of the GT₊ channel as discussed earlier. We note that the Fermi contribution to the total ECC is negligible. Because these transitions are already unblocked at T = 5.8 *GK*, a further increase in temperature to T = 17.4 *GK* results in a comparatively small increase (less than a factor two) of the calculated ECC. Fig. 3 (right panel) and Fig. 4 show a similar temperature dependence of pn-QRPA model calculated ECC and its comparison with SMMC results for odd-A nuclei ⁵¹V, ⁵⁵Fe and ⁵⁹Co, respectively. For all remaining cases the SMMC numbers are roughly an order of magnitude bigger at high *w*. We note that the SMMC model invoked a quenching factor of 0.8 in their ECC estimation to be compared with a tighter pn-QRPA quenching factor of 0.6.

Next we show the calculation of ECC for even-even nuclei. Several nuclear models, including the SMMC [10], the pn-QRPA model with a Bonn C-D potential [1], finite temperature HF+RPA [32], finite temperature relativistic RPA [37], thermal quasiparticle RPA [9] and the hybrid SMMC+RPA model [38], were used in the past, to perform ECC calculation of even-even nuclei. For the case of ⁵⁴Fe, we compare our calculated ECC with the SMMC result [10] and the finite temperature relativistic RPA (FTRRPA) estimation performed by Niu and collaborators [37] in the bottom-left panel of Fig. 5. The FTRRPA calculation was performed up to temperature of 23.2 *GK*. We notice that the electron capture threshold energy remains more or less same in SMMC (at T = 5.8 *GK*) and FTRRPA (at T = 23.2 *GK*) computations. The FTRRPA calculated ECC becomes almost independent of temperature at $w \geq 5$ *MeV*. We notice that the FTRRPA computed ECC is a factor 2-3 bigger than the SMMC results. The pn-QRPA calculated threshold is somewhat lower. At low *w*, our ECC is 2-3 orders of magnitude smaller than FTRRPA results but at high *w* the two estimations are in good comparison. The SMMC results are roughly a factor three bigger at high *w*. Right panels of Fig. 5 compare our ECC calculation with those of SMMC for the even-even nucleus ⁵⁸Fe. We note that at $w = 29.1$ *MeV* the pn-QRPA computed ECC is roughly a factor 8 bigger than SMMC despite a much tighter quenching factor used in our calculation. The most probable reason for this enhancement could be that SMMC computation is carried out in the $0\hbar\omega$ *fp*-shell space. On the other hand we perform our pn-QRPA calculation in a $7\hbar\omega$ model space so that for any multipole operator the whole sum rule is exhausted, whereas, generally speaking, this is not the case in SMMC calcu-

lation.

Fig. 6 depicts our ECC estimation for odd-odd nuclei $^{56,58}\text{Mn}$. The upper panel of Fig. 6 shows our estimated ECC for ^{56}Mn . At low w of 2.5 MeV the ECC for ^{56}Mn is around a factor 4 bigger than for ^{58}Mn (lower panel) for $T = 5.8\text{ GK}$. The temperature evolution is very much similar to that for other cases. The estimated GT strength distribution for ground and first two excited states of ^{56}Mn were presented earlier in Fig. 2. The NPFs for $^{56,58}\text{Mn}$ used in the calculation can be seen in Table II.

Table IV investigates how the two different values of pairing gaps, determined in our model, effect the calculated ECC. Here we show the calculated ECC for all nine fp -shell nuclei using Scheme-I and Scheme-II. The calculated ECC for the two schemes are shown as a function of incident electron energy. We note that the calculated ECC do not differ significantly for the two schemes. The Scheme-I ECC were bigger at most by a factor 2.5 for the case of ^{58}Mn at $w = 2\text{ MeV}$ while the Scheme-II ECC were at most a factor 1.5 bigger for the case of ^{56}Mn at $w = 10\text{ MeV}$. At low values of w the ECC using Scheme-I is slightly bigger (except for the case of ^{54}Fe). However as w increases the two calculations get in better agreement. Due to a small number of nuclei investigated in this study, we are not in a position to determine which set of pairing gaps gives better results. We intend to investigate this more as a future assignment.

We next present some results of stellar electron capture rates for fp -shell nuclei. To this purpose we earmark three values of stellar density (10^4 g/cm^3 , 10^8 g/cm^3 and 10^{11} g/cm^3) representing low, medium and regions of high stellar density, respectively. We adopted the prescription of Martin and Bleichert-Toft [39] for the calculation of phase space functions for electron capture. We present total phase space of ^{45}Sc , ^{56}Mn , ^{58}Fe and ^{59}Co as a function of stellar temperature in Fig. 7. Each panel shows three curves representing the three selected stellar densities. The phase space increases with increasing stellar temperature and density. For low and intermediate densities the phase space is essentially zero at small stellar temperature of 0.01 GK and increases with increasing temperatures. For high density regions, the phase space is $\sim 10^9$ at 0.01 GK and increases to $\sim 10^{11}$ at 30 GK .

The pn-QRPA calculated stellar electron capture rates for ^{45}Sc and ^{59}Co is presented in Fig. 8. Shown also are the results of large scale shell model (LSSM) [3] and the independent particle model (IPM) [2] calculations. The comparison is presented over three panels depicting low, medium and high stellar densities, respectively. At low stellar density the three computations are in excellent agreement. At 30 GK , our calculated rates are 41 s^{-1} , to be compared with 20 s^{-1} (IPM) and 10 s^{-1} (LSSM). At intermediate density, pn-QRPA rates are slightly smaller at low temperatures. At 30 GK , we have more or less the same comparison. At high density and low temperature IPM results are around two orders of magnitude bigger than pn-QRPA and LSSM rates. At 30 GK ,

the pn-QRPA calculation is around factor 3 bigger than IPM rates. LSSM rates are again small at high temperatures. The Lanczos-based approach employed in LSSM calculation may explain the source of these small rates. These were first highlighted by Pruet and Fuller [40]. The Lanczos iterations essential for convergence in rate calculation and the corresponding behavior of partition functions may get affected and consequently the LSSM rates tend to be too low at high temperatures. The pn-QRPA calculation, not Lanczos-based in nature, do not suffer from this convergence problem. At high temperatures, where the occupation probability of excited states is larger, our EC rates are accordingly enhanced compared to LSSM and IPM rates.

The left panel of Fig. 9 shows pn-QRPA estimated electron capture rates and comparison with IPM and LSSM rates on ^{56}Mn . At low stellar density the comparison with previous calculations is akin to the case of ^{45}Sc . At intermediate density the pn-QRPA rates are around one order of magnitude bigger at all temperatures whereas at high density the comparison is once again similar to what we witnessed for the case of ^{45}Sc (for further detail see Ref. [41]). Unmeasured matrix elements were assigned an average value of $\log ft = 5$ in IPM calculation for allowed transitions. On the other hand these transitions were computed in a microscopic fashion using the pn-QRPA and LSSM approaches thereby increasing the reliability of the calculated rates.

We finally depict the electron capture rates for the even-even nucleus ^{58}Fe and comparison with previous calculations in right panel of Fig. 9. The LSSM rates are around a factor 2 – 3 smaller at high temperatures for reason already mentioned. At high stellar density the IPM rates are bigger for all temperatures. IPM threshold parent excitation energies were not constrained and extended well beyond the particle decay channel taken into account in the current model. At high temperatures contributions from these high excitation energies begin to show their cumulative effect. The IPM rates are usually bigger than the pn-QRPA and LSSM rates, specially at high stellar density. The misplacement of GT centroid (for further details on centroid placement in LSSM and IPM calculations see Refs. [3, 42]), assignment of an average value of $\log ft = 5$ for all unmeasured transitions and performing sum on parent excitation energies well beyond the particle decay channel could be the probable reasons for this enhancement in IPM rates. The pn-QRPA model provides an adequate model space that can effectively handle all the excited states in parent as well as in daughter nuclei. We do not consider the Brink-Axel hypothesis in our calculation to approximate the EC rate contribution from parent excited levels. This approximation was used both by IPM and LSSM. Accordingly, whenever rates from ground state command the total rate, our electron capture rates are in decent agreement with previous calculations. For cases where excited state partial rates influence the total rate, differences are seen between the pn-QRPA and previous results.

The influence of pairing gap values on EC rates is explored in Table V. Here we calculate EC at fixed stellar densities of 10 g/cm^3 , 10^4 g/cm^3 and 10^8 g/cm^3 and core temperatures of 5 GK , 25 GK and 30 GK for the two pairing gap schemes for all nine nuclei. Once again we notice that there is no significant change in the calculated EC values for the two different schemes. As the core temperature increases we note that the EC rates calculated using pairing gap values of Scheme-II increase. We are currently working on the role of pairing correlations in calculation of β -decay half-lives [45] where we investigate in detail which scheme results in a better prediction of calculated half-life values using the pn-QRPA model. Our preliminary results favor the use of Scheme-II.

IV. SUMMARY AND CONCLUSION

We presented a microscopic calculation of GT strength distributions for key fp -shell nuclei from ground and excited states of the parent nucleus. Our results were indicative of the fact that Brink-Axel hypothesis may not be a good approximation to be used for the estimation of stellar weak rates. The computed NPFs emphasized on the treatment of nuclear excited states as *discrete* up to 10 MeV . The energy levels were calculated by solving the relevant BCS equations which gave us the quasiparticle energies and probabilities for each particle level to be (un)occupied. The resulting NPFs showed considerable differences when compared with those calculated using traditional recipes.

We calculated ECC for even-even, odd-A and odd-odd fp -shell nuclei. We used the pn-QRPA model in a multi-shell single-particle space with a schematic interaction to estimate ECC for fp -shell nuclei of astrophysical significance. The temperature dependence of ECC was explored. As the temperature increased from 5.8 GK to 11.6 GK , we calculated a noticeable increase, up to an order of magnitude, in the ECC corresponding to a significant thermal unblocking of the GT^+ channel. There was a marginal increase in the computed ECC when the core temperature was raised further. At low incident electron energies, our calculated ECC was systematically smaller than SMMC results which we attribute to the strong configuration mixing in SMMC calculation and a tighter quenching factor adopted in

our model. For high incident energies shell model results are factor eight (two) smaller for ^{58}Fe (^{45}Sc).

The pn-QRPA calculated electron capture rates for fp -shell nuclei in stellar matter were shown. These were, in general, found to be bigger than previous estimations at high stellar temperatures. The ASCII files of all computed stellar rates, on a fine temperature-density grid suitable for interpolation purposes, are available and may be requested from the authors.

The role of empirical pairing gap for protons and neutrons on calculated ECC and EC rates was investigated. In first instance the pairing gaps were taken to be the same for protons and neutrons (Scheme-I). Later we used pairing gaps using 3-point formula (Scheme-II). The latter are argued to be more accurate. The calculated EC rates using Scheme-II were slightly bigger at high core temperatures. For low incident electron energies the calculated ECC is slightly bigger using pairing gaps from Scheme-I. As w increases the two calculations get in better agreement.

The ECC calculation and associated EC rates presented in this paper have many astrophysical applications. They can be used for estimating neutrino-spectra arising from electron capture on nuclei during supernova phase. One needs the neutrino-spectra in the stellar core, as a function of position and time, for modeling and simulation of the presupernova and supernova phases of massive stars. The energy loss rates due to supernova neutrinos may determine a specific supernova-neutrino scenario. One can estimate the neutrino emissivity using the neutrino-spectra (see e.g. [3]). The inverse neutrino absorption process can be determined using the EC rates presented in this work and would be taken as a future assignment. In future we plan to investigate role of forbidden transitions in calculation of ECC, specially at high electron incident energies.

J.-U. Nabi would like to acknowledge the support of the Higher Education Commission Pakistan through project numbers 5557/KPK/NRPU/R&D/HEC/2016 and 9-5(Ph-1-MG-7)Pak-Turk/R&D/HEC/2017 and Pakistan Science Foundation through project number PSF-TUBITAK/KP-GIKI (02).

-
- [1] P. G. Giannaka and T. S. Kosmas, Adv. High Energy Phy. **2015**, Article ID 398796 (2015).
 - [2] G. M. Fuller, W. A. Fowler, and M. J. Newman, Astrophys. J. Suppl. Ser. **42**, 447 (1980); **48**, 279 (1982); Astrophys. J. **252**, 715 (1982); **293**, 1 (1985).
 - [3] K. Langanke and G. Martínez-Pinedo, Nucl. Phys. A **673**, 481 (2000).
 - [4] D. Brink, D. Phil. Thesis, Oxford University, Unpublished (1955); P. Axel, Phys. Rev. **126**, 671 (1962).
 - [5] K. Kar, A. Ray, and S. Sarkar, Astrophys. J. **434**, 662 (1994).
 - [6] J.-U. Nabi and H. V. Klapdor-Kleingrothaus, Eur. Phys. J. A **5**, 337-339 (1999).
 - [7] J.-U. Nabi and H. V. Klapdor-Kleingrothaus, At. Data Nucl. Data Tables **71**, 149-345 (1999).
 - [8] J.-U. Nabi and H. V. Klapdor-Kleingrothaus, At. Data Nucl. Data Tables **88**, 237-476 (2004).
 - [9] A. A. Dzhoiev, A. I. Vdovin, V. Yu. Ponomarev, J.

- Wambach, K. Langanke and G. Martínez-Pinedo, Phys. Rev. C **81**, 015804 (2010).
- [10] D. J. Dean, K. Langanke, L. Chatterjee, P. B. Radha, and M. R. Strayer, Phys. Rev. C **58**, 536 (1998).
- [11] T. Fischer, M. Hempel, I. Sagert, Y. Suwa and J. Schaffner-Bielich, Eur. Phys. J. A. **50**, 1 (2014).
- [12] M. B. Aufderheide, I. Fushiki, S. E. Woosley, E. Stanford, D. H. Hartmann, Astrophys. J. Suppl. Ser. **91**, 389 (1994).
- [13] W. R. Hix and F.-K. Thielemann, Astrophys. J. **460**, (1996) 869.
- [14] T. Rauscher and F.-K. Thielemann, At. Data Nucl. Data Tables **75** (2000) 1.
- [15] P. Möller, J. R. Nix, W. D. Myers and W. J. Swiatecki, At. Data Nucl. Data Tables **59** (1995) 185.
- [16] J. M. Pearson, R. C. Nayak and S. Goriely, Phs. Lett. B **387** (1996) 455.
- [17] T. Rauscher, Astro. J. Supp. Ser. **147** (2003) 403.
- [18] A. Dimarco, C. Barbero, H. Dias, F. Garcia, J. Horvath and L. Losano, J. Phys. G **28**, 121 (2002).
- [19] J.-U. Nabi, A. N. Tawfik, N. Ezzelarab and A. A. Khan, Astrophys. Space Sci. **361**, 1-9 (2016).
- [20] J.-U. Nabi, A. N. Tawfik, N. Ezzelarab and A. A. Khan, Physica Scripta (2016).
- [21] S. G. Nilsson, Mat. Fys. Medd. Dan. Vidensk. Selsk. **29**, 16 (1955).
- [22] J.-U. Nabi, M. U. Rehman and M. Sajjad, Braz. J. Phys **37**, 1238-1245 (2007).
- [23] I. Ragnarsson and R. K. Sheline, Phys. Scr. **29**, 385 (1984).
- [24] G. Audi, F. G. Kondev, M. Wang, W. J. Huang and S. Naimi, Chin. phys. C **41**,030001 (2017).
- [25] A. Bohr and B. R. Mottelson, Nuclear Structure, World Scientific **1**, (1998).
- [26] P. Möller, A. J. Sierk, T. Ichikawa and H. Sagawa, At. Data Nucl. Data Tables **109** 1-204 (2016).
- [27] M. Hirsch, A. Staudt, K. Muto and H. V. KlapdorKleingrothaus, At. Data and Nucl. Data Tables **53**, 165-193 (1993).
- [28] M. Hirsch, A. Staudt, K. Muto and H. V. KlapdorKleingrothaus, Nucl. Phys. A **535**, 62 (1991).
- [29] K. Muto, E. Bender, and H. V. Klapdor, Z. Phys. A **333**, 125 (1989).
- [30] A. Bohr, B. R. Mottelson, Nuclear Structure, World Scientific, **1** 1969.
- [31] J. D. Walecka, Theoretical nuclear and subnuclear physics, World Scientific, London, (2004).
- [32] N. Paar, G. Colò, E. Khan, and D. Vretenar, Phys. Rev. C **80**, 055801 (2009).
- [33] C. D. Goodman, C. A. Goulding, M. B. Greenfield, J. Rapaport, D. E. Bainum, C. C. Foster, W. G. Love and F. Petrovich, Phy. Rev. Lett **44**, 1755 (1980).
- [34] N. B. Gove and M. J. Martin, Nucl. Data Tables **10**, 205-317 (1971).
- [35] C. Gaarde, Nucl. Phys. A **396** 127c 1983.
- [36] J. C. Hardy, and I. S. Towner, Phys. Rev. C **79**, 055502 (2009).
- [37] Y. F. Niu, N. Paar, D. Vretenar and J. Meng, Phys. Rev. C **83**, 045807 (2011).
- [38] K. Langanke, E. Kolbe, D.-J. Dean, Phy. Rev. C **63**, 032801 (2001).
- [39] M. J. Martin and P. H. Blichert-Toft, Nucl. Data Tables **A8**, 1-198 (1970).
- [40] J. Pruet and G. M. Fuller, Astrophys. J. Suppl. Ser. **149** 189-203 (2003).
- [41] M. Majid, J.-U. Nabi, and M. Riaz. Int. J. Mod. Phys. E, **27** 1850019 (2018).
- [42] K. Langanke and G. Martínez-Pinedo, At. Data Nucl. Data Tables **79**, 1-46 (2001).
- [43] W. P. Alford, B. A. Brown, S. Burzynski, A. Celler, Phys. Rev. C **48**, 2818 (1993).
- [44] M. S. Freedman, F. T. Porter and Jr. F. Wagner, Phy. Rev **140**, B563 (1965).
- [45] J.-U. Nabi and M. Ishfaq (in preparation)
- [46] K. Muto, E. Bender, T. Oda and H. V. Klapdor-Kleingrothaus, Z. Phys. A **341**, 407 (1992).

V. APPENDIX A

Excited states of even-even nucleus were obtained by invoking one-proton (or one-neutron) excitations. They were described, in the quasiparticle (q.p.) picture, by adding two-proton (two-neutron) q.p.'s to the ground state [46]. Allowed transitions from these initial states to final proton-neutron q.p. pair states in the odd-odd daughter nucleus were calculated keeping in mind the selection rules. The transition amplitudes and their reduction to correlated (*c*) one-q.p. states [46] were given by

$$\begin{aligned} \langle p^f n_c^f | \tau^+ \sigma_{-\mu} | p_1^i p_{2c}^i \rangle = & -\delta(p^f, p_2^i) \langle n_c^f | \tau^+ \sigma_{-\mu} | p_{1c}^i \rangle \\ & + \delta(p^f, p_1^i) \langle n_c^f | \tau^+ \sigma_{-\mu} | p_{2c}^i \rangle \end{aligned} \quad (1A)$$

$$\begin{aligned} \langle p^f n_c^f | \tau^+ \sigma_{\mu} | n_1^i n_{2c}^i \rangle = & +\delta(n^f, n_2^i) \langle p_c^f | \tau^+ \sigma_{\mu} | n_{1c}^i \rangle \\ & -\delta(n^f, n_1^i) \langle p_c^f | \tau^+ \sigma_{\mu} | n_{2c}^i \rangle, \end{aligned} \quad (25)$$

where τ^+ are the isospin raising operators ($\tau^+ | p \rangle = | n \rangle$) and $\vec{\sigma}$ is the Pauli spin operator. Four-proton (four-neutron) and higher q.p. states were not considered in the model and may be taken as a future task.

For odd-A nuclei low-lying states were obtained by lifting the q.p. in the orbit of the smallest energy to higher-lying orbits [46]. The excited states were constructed by following three mechanisms

- (i) lifting the odd neutron (proton) from ground state to excited states,
- (ii) three-neutron (three-proton) states, corresponding to excitation of a neutron (proton), or,
- (iii) one-neutron two-proton (one-proton two-neutron) states, corresponding to excitation of a proton (neutron).

The reduction of multi-q.p. transitions to correlated (*c*) one-q.p. states were given by,

$$\begin{aligned} \langle p_1^f n_1^f n_{2c}^f | \tau^+ \sigma_{\mu} | n_1^i n_2^i n_{3c}^i \rangle = & \delta(n_1^f, n_2^i) \delta(n_2^f, n_3^i) \\ \langle p_{1c}^f | \tau^+ \sigma_{\mu} | n_{1c}^i \rangle - \delta(n_1^f, n_1^i) \delta(n_2^f, n_3^i) \langle p_{1c}^f | \tau^+ \sigma_{\mu} | & n_{2c}^i \rangle \\ & + \delta(n_1^f, n_1^i) \delta(n_2^f, n_2^i) \langle p_{1c}^f | \tau^+ \sigma_{\mu} | n_{3c}^i \rangle \end{aligned} \quad (26)$$

$$\begin{aligned}
& \langle p_1^f n_1^f n_{2c}^f | \tau^+ \sigma_{-\mu} | p_1^i p_2^i n_{1c}^i \rangle = \delta(p_1^f, p_2^i) [\delta(n_1^f, n_1^i) \\
& \langle n_{2c}^f | \tau^+ \sigma_{-\mu} | p_{1c}^i \rangle - \delta(n_2^f, n_1^i) \langle n_{1c}^f | \tau^+ \sigma_{-\mu} | p_{1c}^i \rangle] \\
& \quad - \delta(p_1^f, p_1^i) [\delta(n_1^f, n_1^i) \langle n_{2c}^f | \tau^+ \sigma_{-\mu} | p_{2c}^i \rangle \\
& \quad - \delta(n_2^f, n_1^i) \langle n_{1c}^f | \tau^+ \sigma_{-\mu} | p_{2c}^i \rangle] \quad (27)
\end{aligned}$$

$$\begin{aligned}
& \langle p_1^f p_2^f p_{3c}^f | \tau^+ \sigma_{\mu} | p_1^i p_2^i n_{1c}^i \rangle = \delta(p_2^f, p_1^i) \delta(p_3^f, p_2^i) \\
& \langle p_{1c}^f | \tau^+ \sigma_{\mu} | n_{1c}^i \rangle - \delta(p_1^f, p_1^i) \delta(p_3^f, p_2^i) \langle p_{2c}^f | \tau^+ \sigma_{\mu} \\
& \quad | n_{1c}^i \rangle + \delta(p_1^f, p_1^i) \delta(p_2^f, p_2^i) \langle p_{3c}^f | \tau^+ \sigma_{\mu} | n_{1c}^i \rangle \quad (28) \\
& \langle p_1^f p_2^f n_{1c}^f | \tau^+ \sigma_{-\mu} | p_1^i p_2^i p_{3c}^i \rangle = \delta(p_1^f, p_2^i) \delta(p_2^f, p_3^i) \langle n_{1c}^f \\
& | \tau^+ \sigma_{-\mu} | p_{1c}^i \rangle - \delta(p_1^f, p_1^i) \delta(p_2^f, p_3^i) \langle n_{1c}^f | \tau^+ \sigma_{-\mu} | p_{2c}^i \rangle \\
& \quad + \delta(p_1^f, p_1^i) \delta(p_2^f, p_2^i) \langle n_{1c}^f | \tau^+ \sigma_{-\mu} | p_{3c}^i \rangle \quad (29)
\end{aligned}$$

$$\begin{aligned}
& \langle p_1^f p_2^f n_{1c}^f | \tau^+ \sigma_{\mu} | p_1^i n_1^i n_{2c}^i \rangle = \delta(n_1^f, n_2^i) [\delta(p_1^f, p_1^i) \langle p_{2c}^f \\
& | \tau^+ \sigma_{\mu} | n_{1c}^i \rangle - \delta(p_2^f, p_1^i) \langle p_{1c}^f | \tau^+ \sigma_{\mu} | n_{1c}^i \rangle] - \delta(n_1^f, \\
& \quad n_1^i) [\delta(p_1^f, p_1^i) \langle p_{2c}^f | \tau^+ \sigma_{\mu} | n_{2c}^i \rangle - \delta(p_2^f, p_1^i) \\
& \quad \langle p_{1c}^f | \tau^+ \sigma_{\mu} | n_{2c}^i \rangle] \quad (30)
\end{aligned}$$

$$\begin{aligned}
& \langle n_1^f n_2^f n_{3c}^f | \tau^+ \sigma_{-\mu} | p_1^i n_1^i n_{2c}^i \rangle = \delta(n_2^f, n_1^i) \delta(n_3^f, n_2^i) \langle n_{1c}^f \\
& | \tau^+ \sigma_{-\mu} | p_{1c}^i \rangle - \delta(n_1^f, n_1^i) \delta(n_3^f, n_2^i) \langle n_{2c}^f | \tau^+ \sigma_{-\mu} | p_{1c}^i \rangle \\
& \quad + \delta(n_1^f, n_1^i) \delta(n_2^f, n_2^i) \langle n_{3c}^f | \tau^+ \sigma_{-\mu} | p_{1c}^i \rangle
\end{aligned}$$

For an odd-odd nucleus the ground state was assumed to be a proton-neutron q.p. pair state of smallest energy. Low-lying states were expressed in the q.p. picture by proton-neutron pair states (two-q.p. states) or by states which were obtained by adding two-proton or two-neutron q.p.'s (four-q.p. states) [46]. Reduction of two-q.p. states into correlated (c) one-q.p. states was given as

$$\begin{aligned}
& \langle p_1^f p_{2c}^f | \tau^+ \sigma_{\mu} | p^i n_c^i \rangle = \delta(p_1^f, p^i) \langle p_{2c}^f | \tau^+ \sigma_{\mu} | n_c^i \rangle \\
& \quad - \delta(p_2^f, p^i) \langle p_{1c}^f | \tau^+ \sigma_{\mu} | n_c^i \rangle \quad (32)
\end{aligned}$$

$$\begin{aligned}
& \langle n_1^f n_{2c}^f | \tau^+ \sigma_{-\mu} | p^i n_c^i \rangle = \delta(n_2^f, n^i) \langle n_{1c}^f | \tau^+ \sigma_{-\mu} | p_c^i \rangle \\
& \quad - \delta(n_1^f, n^i) \langle n_{2c}^f | \tau^+ \sigma_{-\mu} | p_c^i \rangle \quad (33)
\end{aligned}$$

while the four-q.p. states were simplified as

$$\begin{aligned}
& \langle p_1^f p_2^f n_1^f n_{2c}^f | \tau^+ \sigma_{-\mu} | p_1^i p_2^i p_3^i n_{1c}^i \rangle = \delta(n_2^f, n_1^i) [\delta(p_1^f, p_1^i) \\
& \delta(p_2^f, p_3^i) \langle n_{1c}^f | \tau^+ \sigma_{-\mu} | p_{1c}^i \rangle - \delta(p_1^f, p_1^i) \delta(p_2^f, p_3^i) \langle n_{1c}^f \\
& | \tau^+ \sigma_{-\mu} | p_{2c}^i \rangle + \delta(p_1^f, p_1^i) \delta(p_2^f, p_2^i) \langle n_{1c}^f | \tau^+ \sigma_{-\mu} | p_{3c}^i \rangle] \\
& \quad - \delta(n_1^f, n_1^i) [\delta(p_1^f, p_2^i) \delta(p_2^f, p_3^i) \langle n_{2c}^f | \tau^+ \sigma_{-\mu} | p_{1c}^i \rangle \\
& \quad - \delta(p_1^f, p_1^i) \delta(p_2^f, p_3^i) \langle n_{2c}^f | \tau^+ \sigma_{-\mu} | p_{2c}^i \rangle + \delta(p_1^f, p_1^i) \delta(p_2^f, \\
& \quad p_2^i) \langle n_{2c}^f | \tau^+ \sigma_{-\mu} | p_{3c}^i \rangle] \quad (34)
\end{aligned}$$

$$\begin{aligned}
& \langle p_1^f p_2^f p_3^f p_{4c}^f | \tau^+ \sigma_{\mu} | p_1^i p_2^i p_3^i n_{1c}^i \rangle = \\
& = -\delta(p_2^f, p_1^i) \delta(p_3^f, p_2^i) \delta(p_4^f, p_3^i) \langle p_{1c}^f | \tau^+ \sigma_{\mu} | n_{1c}^i \rangle \\
& \quad + \delta(p_1^f, p_1^i) \delta(p_3^f, p_2^i) \delta(p_4^f, p_3^i) \langle p_{2c}^f | \tau^+ \sigma_{\mu} | n_{1c}^i \rangle \\
& \quad - \delta(p_1^f, p_1^i) \delta(p_2^f, p_2^i) \delta(p_4^f, p_3^i) \langle p_{3c}^f | \tau^+ \sigma_{\mu} | n_{1c}^i \rangle \\
& \quad + \delta(p_1^f, p_1^i) \delta(p_2^f, p_2^i) \delta(p_3^f, p_3^i) \langle p_{4c}^f | \tau^+ \sigma_{\mu} | n_{1c}^i \rangle \quad (35)
\end{aligned}$$

$$\begin{aligned}
& \langle p_1^f p_2^f n_1^f n_{2c}^f | \tau^+ \sigma_{\mu} | p_1^i n_1^i n_2^i n_{3c}^i \rangle = \delta(p_1^f, p_1^i) [\delta(n_1^f, n_2^i) \\
& \delta(n_2^f, n_3^i) \langle p_{2c}^f | \tau^+ \sigma_{\mu} | n_{1c}^i \rangle - \delta(n_1^f, n_1^i) \delta(n_2^f, n_3^i) \\
& \langle p_{2c}^f | \tau^+ \sigma_{\mu} | n_{2c}^i \rangle + \delta(n_1^f, n_1^i) \delta(n_2^f, n_2^i) \langle p_{2c}^f | \tau^+ \sigma_{\mu} \\
& \quad | n_{3c}^i \rangle] - \delta(p_2^f, p_1^i) [\delta(n_1^f, n_2^i) \delta(n_2^f, n_3^i) \\
& \langle p_{1c}^f | \tau^+ \sigma_{\mu} | n_{1c}^i \rangle - \delta(n_1^f, n_1^i) \delta(n_2^f, n_3^i) \langle p_{1c}^f | \tau^+ \sigma_{\mu} \\
& \quad | n_{2c}^i \rangle + \delta(n_1^f, n_1^i) \delta(n_2^f, n_2^i) \langle p_{1c}^f | \tau^+ \sigma_{\mu} | n_{3c}^i \rangle] \quad (36)
\end{aligned}$$

$$\begin{aligned}
& \langle n_1^f n_2^f n_3^f n_{4c}^f | \tau^+ \sigma_{-\mu} | p_1^i n_1^i n_2^i n_{3c}^i \rangle = \\
& + \delta(n_2^f, n_1^i) \delta(n_3^f, n_2^i) \delta(n_4^f, n_3^i) \langle n_{1c}^f | \tau^+ \sigma_{-\mu} | p_{1c}^i \rangle \\
& \quad - \delta(n_1^f, n_1^i) \delta(n_3^f, n_2^i) \delta(n_4^f, n_3^i) \langle n_{2c}^f | \tau^+ \sigma_{-\mu} | p_{1c}^i \rangle \\
& \quad + \delta(n_1^f, n_1^i) \delta(n_2^f, n_2^i) \delta(n_4^f, n_3^i) \langle n_{3c}^f | \tau^+ \sigma_{-\mu} | p_{1c}^i \rangle \\
& \quad - \delta(n_1^f, n_1^i) \delta(n_2^f, n_2^i) \delta(n_3^f, n_3^i) \langle n_{4c}^f | \tau^+ \sigma_{-\mu} | p_{1c}^i \rangle \quad (37)
\end{aligned}$$

For all the given q.p. transition amplitudes [Eqs. (1A)-(37)], the antisymmetrization of the single- q.p. states was taken into account:

$$\begin{aligned}
& p_1^f < p_2^f < p_3^f < p_4^f, \\
& n_1^f < n_2^f < n_3^f < n_4^f, \\
& p_{1c}^f < p_{2c}^f < p_{3c}^f < p_{4c}^f, \\
& n_{1c}^f < n_{2c}^f < n_{3c}^f < n_{4c}^f.
\end{aligned}$$

GT transitions of phonon excitations for every excited state were also taken into account. In this case it was assumed that the quasiparticles in the parent nucleus remained in the same quasiparticle orbits. For solution of pn-QRPA equation with separable GT forces and construction of reduced transition probabilities please see Ref. [46].

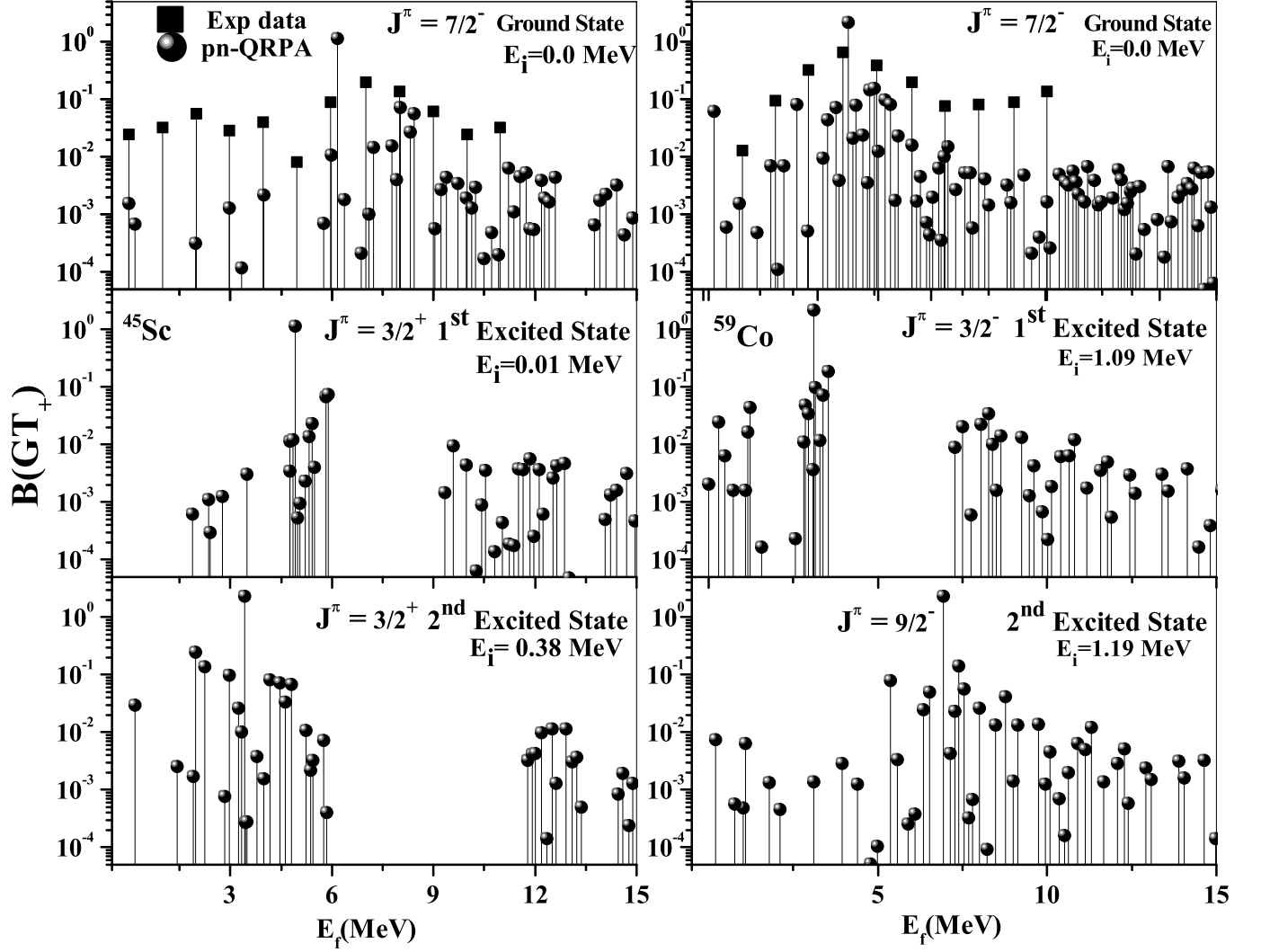


FIG. 1. GT₊ strength distributions calculated using the pn-QRPA theory for the ground and first two excited states of ⁴⁵Sc and ⁵⁹Co. Experimental data were taken from Refs. [43, 44].

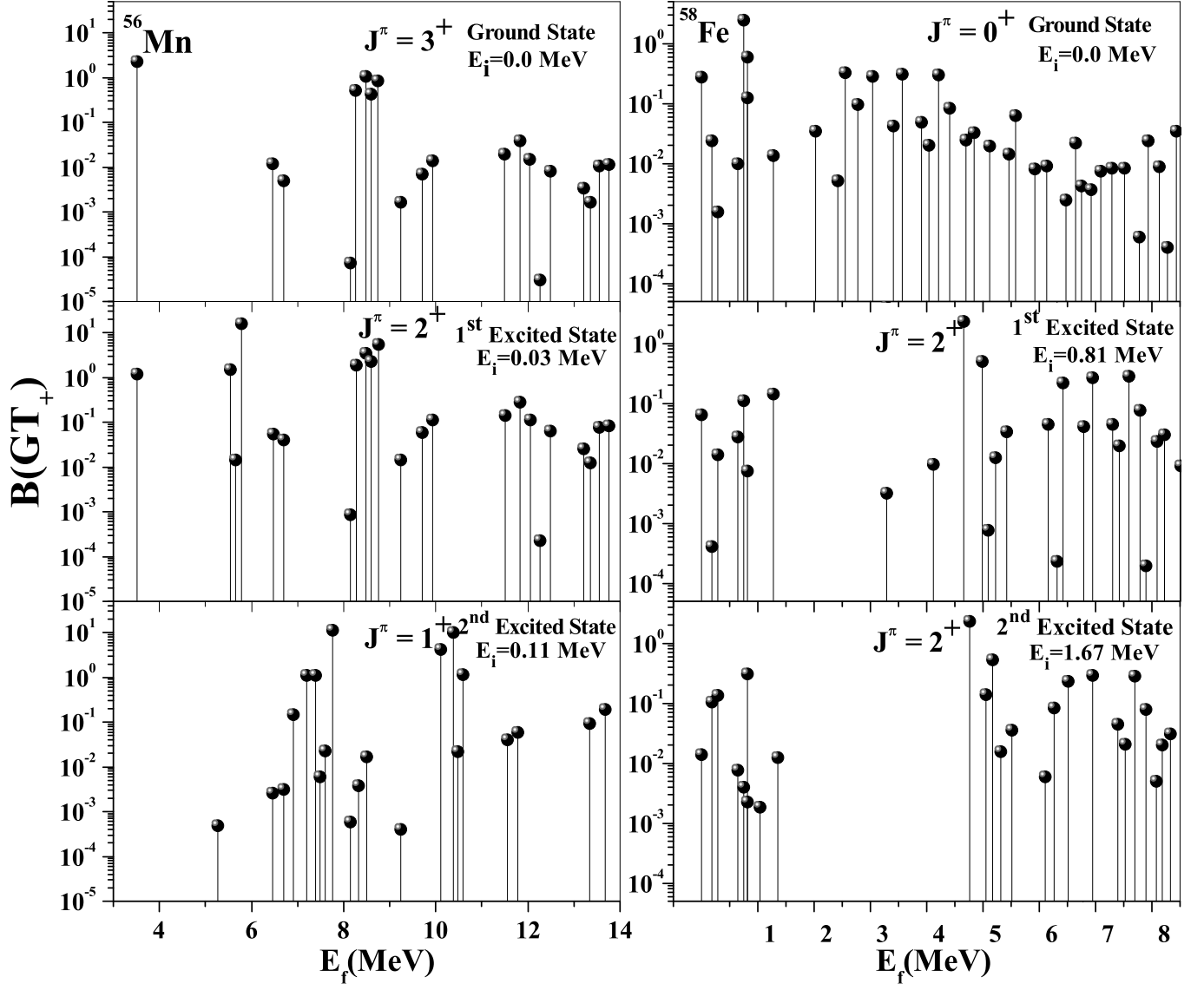


FIG. 2. Same as Fig. 1 but for ^{56}Mn and ^{58}Fe .

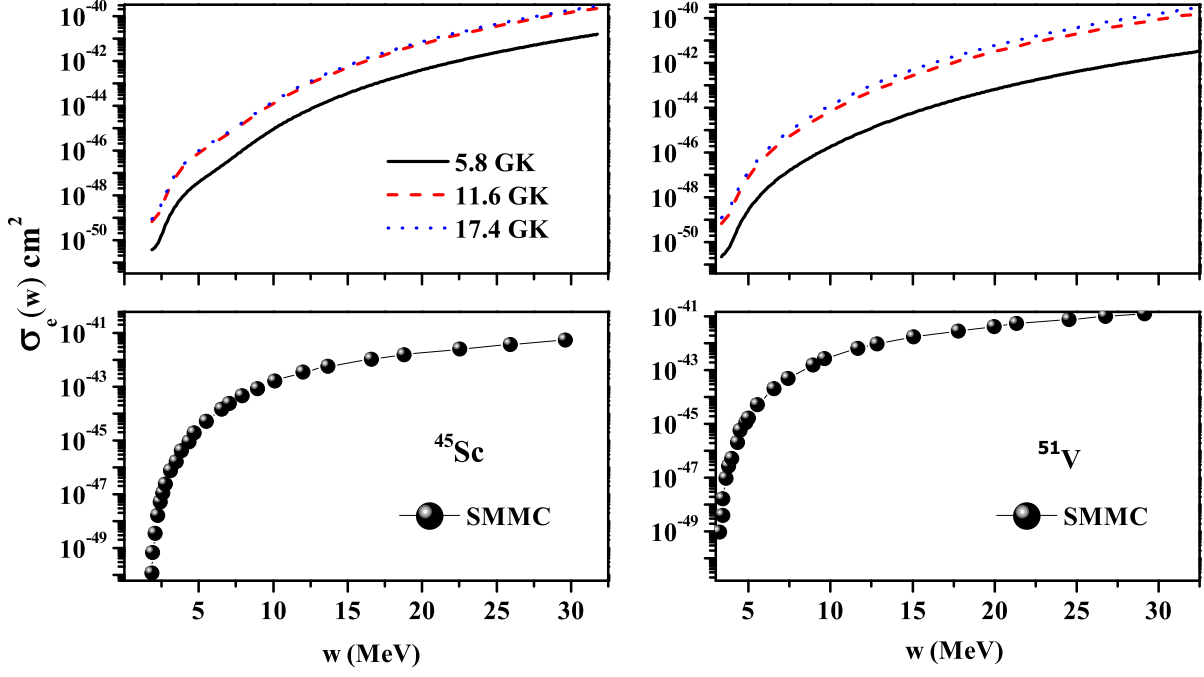


FIG. 3. Electron capture cross sections for ^{45}Sc and ^{51}V , using the pn-QRPA theory, as a function of the incident electron energy (w) at different stellar temperatures. Bottom panels show result of SMMC calculation [10].

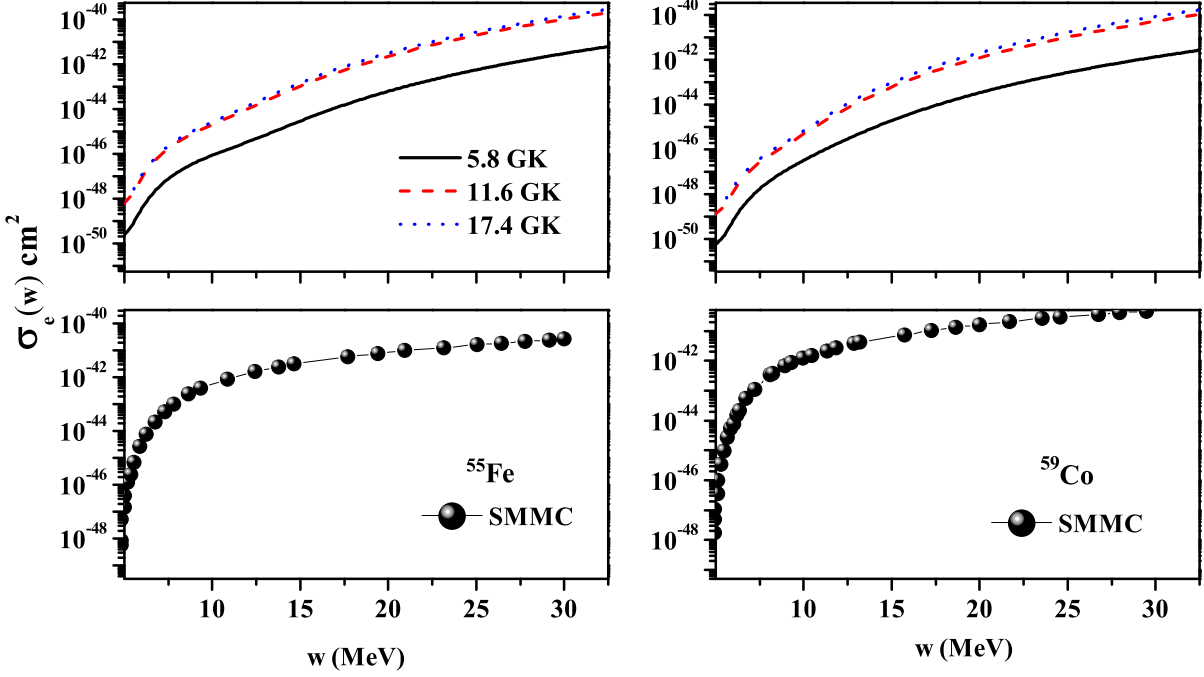


FIG. 4. Same as Fig. 3 but for ^{55}Fe and ^{59}Co .

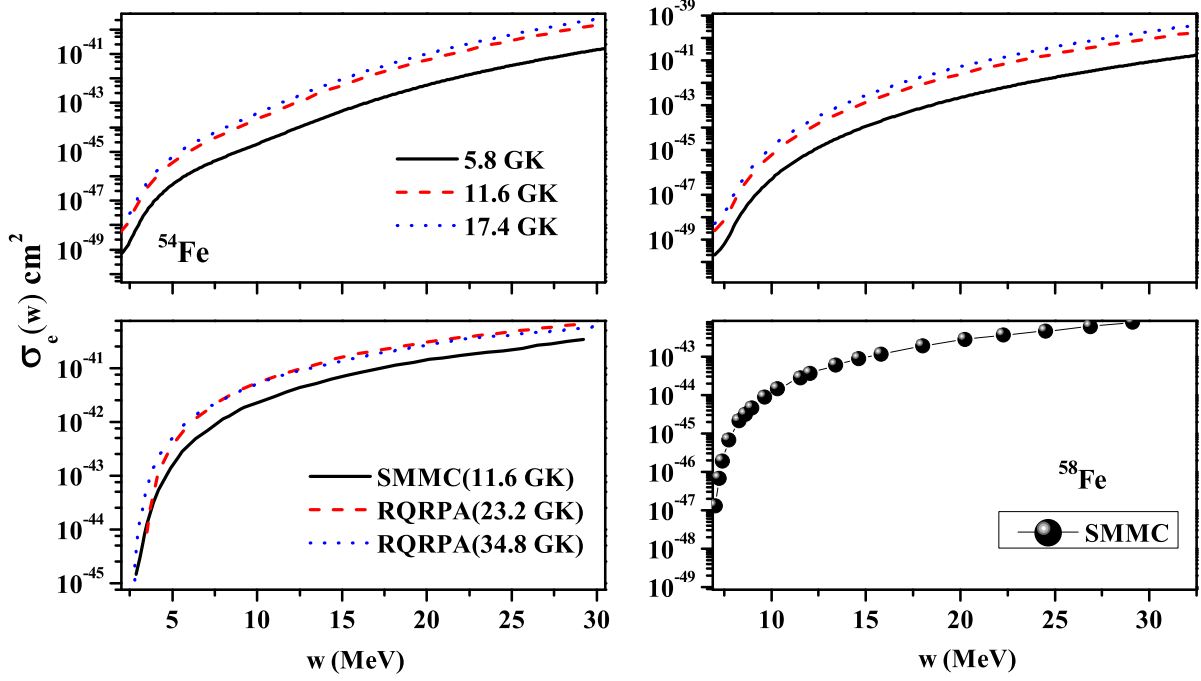


FIG. 5. Same as Fig. 3 but for $^{54,58}\text{Fe}$. Bottom panel shows results of SMMC [10] and FTRRPA calculations [37].

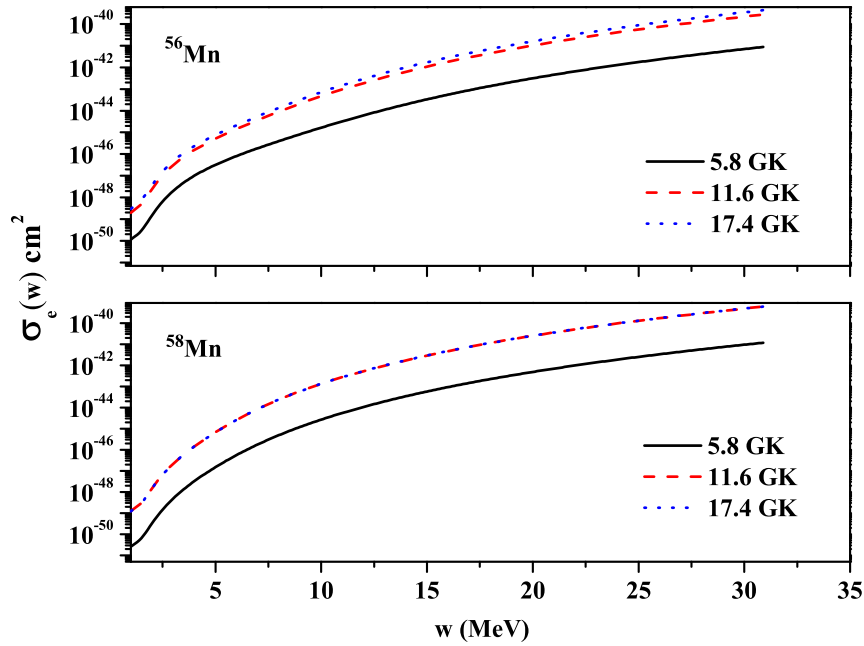


FIG. 6. Pn-QRPA calculated electron capture cross sections for ^{56}Mn (top panel) and ^{58}Mn (bottom panel) as a function of the incident electron energy (w) at different stellar temperatures.

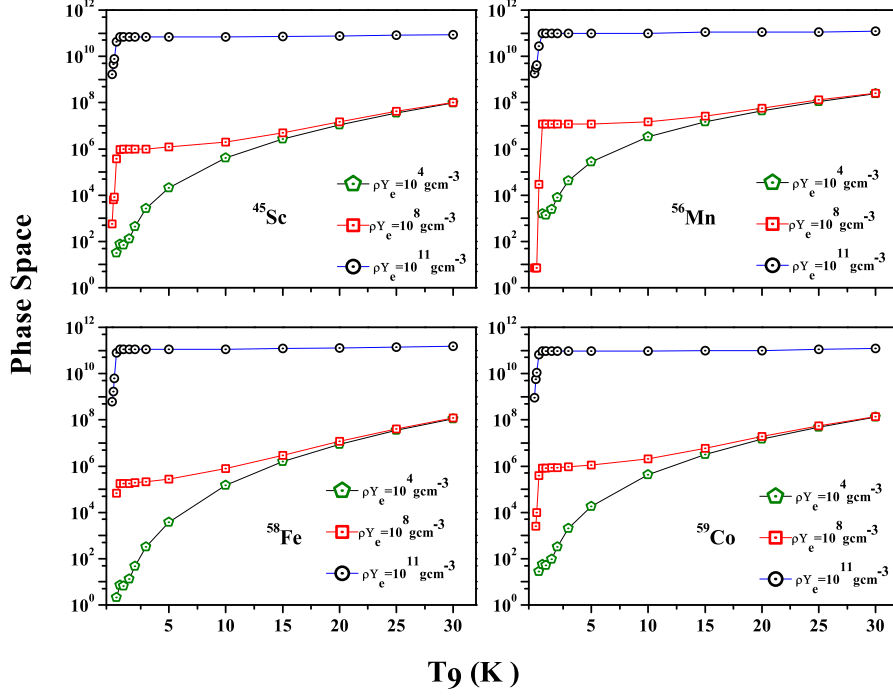


FIG. 7. Total phase space for few fp -shell nuclei as a function of stellar temperature and density.

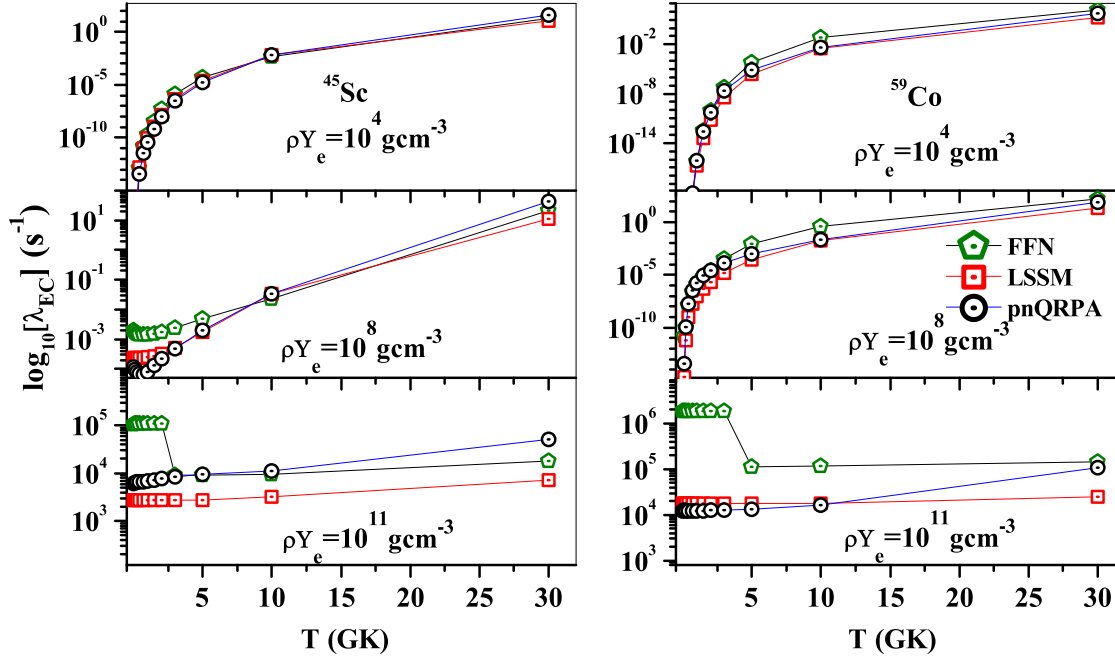


FIG. 8. Comparison of pn-QRPA electron capture rates on ^{45}Sc and ^{59}Co with those calculated by LSSM and IPM as a function of stellar temperature and density.

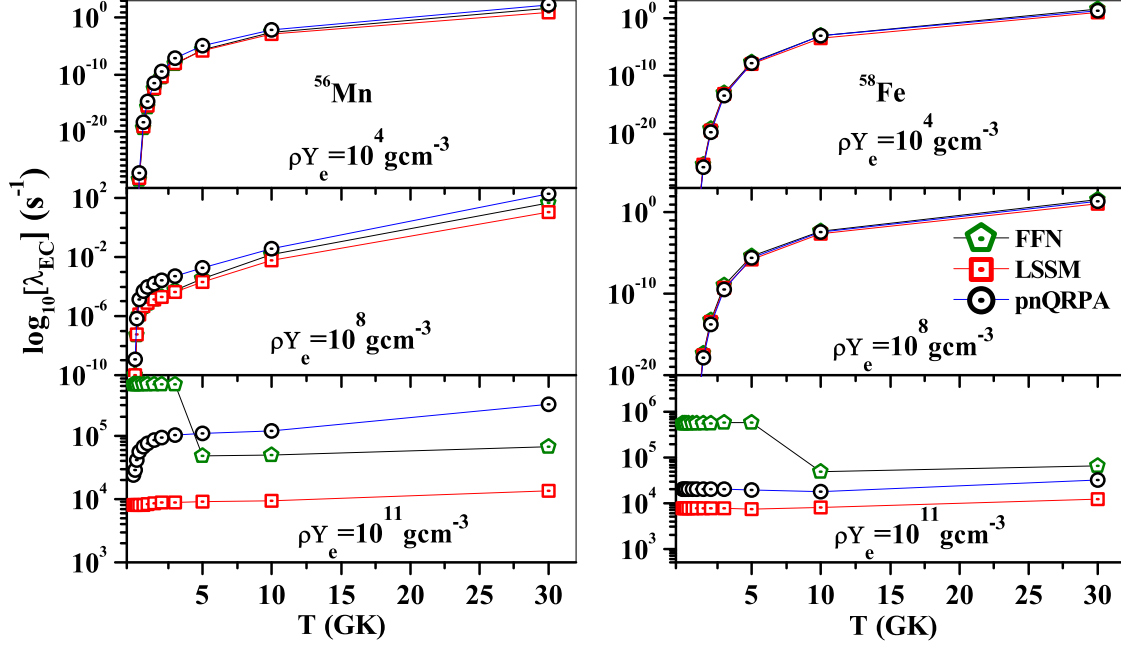


FIG. 9. Same as Fig. 8 but for ^{56}Mn and ^{58}Fe .

TABLE I. Comparison of pairing gaps calculated by traditional formula (Scheme-I) and 3-point formula (Scheme-II).

Nuclei	Scheme-II	
	$\Delta_n = \Delta_p$	$\Delta_n \quad \Delta_p$
^{45}Sc	1.789	1.048 2.186
^{51}V	1.680	1.364 1.635
^{54}Fe	1.633	1.692 1.521
^{55}Fe	1.618	1.495 1.254
^{56}Fe	1.604	1.363 1.568
^{56}Mn	1.604	1.083 1.221
^{58}Mn	1.576	0.897 1.152
^{58}Fe	1.576	1.466 1.765
^{59}Co	1.562	1.211 1.691

TABLE II. Calculated nuclear partition functions for few fp -shell nuclei compared with the earlier statistical calculations of [14, 17] denoted by FRDM. Numbers in parenthesis indicate stellar temperature in units of GK .

Nuclei	pnQRPA G(0.01) G(0.5)	FRDM G(0.01) G(0.5)	pnQRPA G(1.5) G(3.0)	FRDM G(1.5) G(3.0)	pnQRPA G(10.0) G(30.0)	FRDM G(10.0) G(30.0)
⁴⁵ Sc	1.03E+00	1.12E+00	2.08E+00	1.50E+00	8.49E+00	6.58E+00
	1.93E+00	1.38E+00	2.41E+00	1.80E+00	2.11E+04	7.51E+03
⁴⁶ Sc	2.26E+00	1.00E+00	5.25E+01	2.45E+00	1.84E+02	1.26E+01
	3.10E+01	1.45E+00	6.52E+01	3.76E+00	1.02E+05	7.51E+03
⁴⁰ Ti	1.00E+00	1.00E+00	1.00E+00	1.00E+00	1.91E+00	2.42E+00
	1.00E+00	1.00E+00	1.00E+00	1.00E+00	2.10E+03	5.75E+03
⁴¹ Ti	1.00E+00	1.00E+00	1.62E+00	1.02E+00	5.17E+00	3.98E+00
	1.24E+00	1.00E+00	1.79E+00	1.15E+00	1.57E+04	3.74E+03
⁴⁴ V	5.00E+00	1.00E+00	5.71E+00	1.19E+00	2.48E+01	8.15E+00
	5.13E+00	1.03E+00	7.01E+00	1.55E+00	8.84E+04	7.78E+03
⁴⁵ V	1.00E+00	1.00E+00	1.90E+01	1.83E+00	3.31E+01	3.57E+00
	8.45E+00	1.34E+00	2.37E+01	2.16E+00	2.22E+04	6.32E+03
⁵¹ V	8.00E+00	1.00E+00	9.89E+00	1.06E+00	4.16E+01	3.45E+00
	8.42E+00	1.00E+00	1.32E+01	1.24E+00	3.11E+04	1.72E+04
⁴² Cr	1.00E+00	1.00E+00	1.00E+00	1.00E+00	2.04E+00	3.74E+00
	1.00E+00	1.00E+00	1.00E+00	1.00E+00	2.39E+03	1.11E+04
⁴³ Cr	1.00E+00	1.00E+00	1.42E+00	1.04E+00	5.61E+00	4.82E+00
	1.07E+00	1.00E+00	1.65E+00	1.20E+00	1.76E+04	6.23E+03
⁵⁶ Mn	1.00E+00	1.03E+00	1.21E+01	2.36E+00	1.74E+02	1.94E+01
	4.45E+00	1.43E+00	2.80E+01	3.98E+00	2.20E+05	1.73E+05
⁵⁷ Mn	1.00E+00	1.00E+00	2.82E+00	1.53E+00	3.02E+01	1.10E+01
	1.71E+00	1.14E+00	3.83E+00	1.78E+00	4.32E+04	2.65E+05
⁵⁸ Mn	3.00E+00	1.00E+00	1.62E+01	1.25E+00	1.22E+02	1.95E+01
	6.72E+00	1.03E+00	2.91E+01	1.76E+00	2.56E+05	4.18E+05
⁵⁴ Fe	1.00E+00	1.00E+00	1.00E+00	1.00E+00	7.04E+00	5.54E+00
	1.00E+00	1.00E+00	1.02E+00	1.02E+00	3.75E+03	9.60E+04
⁵⁵ Fe	4.00E+00	1.00E+00	4.72E+00	1.02E+00	3.09E+01	6.02E+00
	4.23E+00	1.00E+00	5.65E+00	1.17E+00	3.73E+04	6.21E+04
⁵⁸ Fe	1.00E+00	1.00E+00	1.01E+00	1.01E+00	1.25E+01	1.09E+01
	1.00E+00	1.00E+00	1.23E+00	1.23E+00	4.47E+03	6.99E+05
⁵⁹ Co	8.00E+00	1.00E+00	8.57E+00	1.00E+00	4.99E+01	6.25E+00
	8.17E+00	1.00E+00	9.18E+00	1.03E+00	4.73E+04	2.02E+05
⁵⁶ Zn	1.00E+00	1.00E+00	1.00E+00	1.00E+00	2.84E+00	5.29E+00
	1.00E+00	1.00E+00	1.00E+00	1.00E+00	4.04E+03	1.85E+05
⁵⁷ Zn	8.00E+00	1.00E+00	8.70E+00	1.03E+00	1.64E+01	4.81E+00
	8.31E+00	1.00E+00	9.02E+00	1.16E+00	4.01E+04	5.96E+04
⁶² Ga	1.00E+00	1.00E+00	1.40E+00	3.98E+00	4.73E+01	2.33E+02
	1.02E+00	1.41E+00	3.16E+00	1.01E+01	3.56E+05	7.26E+06
⁶³ Ga	4.00E+00	1.00E+00	7.66E+00	1.26E+00	3.41E+01	2.54E+01
	5.04E+00	1.04E+00	1.07E+01	1.79E+00	6.11E+04	1.96E+06
⁵⁹ Ge	1.00E+00	1.00E+00	1.77E+00	1.05E+00	1.25E+01	7.01E+00
	1.44E+00	1.00E+00	2.03E+00	1.20E+00	4.94E+04	1.30E+05
⁶⁰ Ge	1.00E+00	1.00E+00	1.00E+00	1.00E+00	3.61E+00	6.04E+00
	1.00E+00	1.00E+00	1.00E+00	1.00E+00	4.53E+03	5.67E+05

TABLE III. Same as Tab. II.

Nuclei	pnQRPA G(0.01) G(0.5)	FRDM G(0.01) G(0.5)	pnQRPA G(1.5) G(3.0)	FRDM G(1.5) G(3.0)	pnQRPA G(10.0) G(30.0)	FRDM G(10.0) G(30.0)
⁶⁵ As	1.00E+00 1.02E+00	1.00E+00 1.04E+00	1.26E+00 1.64E+00	1.31E+00 1.92E+00	1.56E+01 6.80E+04	3.13E+01 2.82E+06
⁶⁶ As	1.00E+00 1.36E+00	1.00E+00 1.11E+00	2.17E+00 3.47E+00	1.83E+00 3.61E+00	5.75E+01 4.51E+05	9.45E+01 7.49E+06
⁶⁵ Se	4.00E+00 4.14E+00	1.00E+00 1.11E+00	4.60E+00 5.12E+00	1.80E+00 3.38E+00	2.19E+01 6.67E+04	7.07E+01 7.39E+06
⁶⁶ Se	1.00E+00 1.00E+00	1.00E+00 1.00E+00	1.00E+00 1.00E+00	1.00E+00 1.17E+00	4.91E+00 5.82E+03	2.71E+01 1.11E+07
⁶⁹ Br	1.00E+00 1.03E+00	1.00E+00 1.03E+00	1.33E+00 1.70E+00	1.19E+00 1.57E+00	1.61E+01 7.33E+04	2.03E+01 4.07E+06
⁷⁰ Br	1.00E+00 2.43E+00	1.00E+00 1.08E+00	4.44E+00 6.68E+00	1.60E+00 2.87E+00	7.62E+01 4.13E+05	7.37E+01 1.10E+07
⁶⁹ Kr	1.00E+00 1.14E+00	1.00E+00 1.21E+00	1.55E+00 1.95E+00	2.53E+00 5.53E+00	1.92E+01 7.86E+04	1.32E+02 3.00E+07
⁷⁰ Kr	1.00E+00 1.00E+00	1.00E+00 1.00E+00	1.00E+00 1.00E+00	1.00E+00 2.01E+00	5.39E+00 6.31E+03	4.49E+01 3.80E+07
⁷⁴ Rb	1.00E+00 1.33E+00	1.00E+00 2.10E+00	2.91E+00 6.19E+00	9.14E+00 2.64E+01	9.48E+01 3.74E+05	1.17E+03 4.02E+08
⁷⁵ Rb	4.00E+00 5.87E+00	1.00E+00 1.09E+00	1.01E+01 1.81E+01	1.64E+00 2.94E+00	8.02E+01 1.00E+05	8.79E+01 8.28E+07
⁷³ Sr	4.00E+00 4.39E+00	1.00E+00 1.16E+00	5.30E+00 6.02E+00	2.13E+00 4.35E+00	2.62E+01 9.40E+04	1.16E+02 5.42E+07
⁷⁴ Sr	1.00E+00 1.00E+00	1.00E+00 1.00E+00	1.00E+00 1.00E+00	1.26E+00 2.46E+00	5.64E+00 7.14E+03	6.59E+01 1.24E+08
⁷⁸ Y	1.00E+00 1.08E+00	1.00E+00 1.13E+00	2.38E+00 6.90E+00	1.97E+00 4.05E+00	1.06E+02 3.30E+05	1.67E+02 1.01E+08
⁷⁹ Y	6.00E+00 6.11E+00	1.00E+00 1.05E+00	8.41E+00 1.32E+01	1.35E+00 2.07E+00	6.12E+01 1.24E+05	6.35E+01 1.34E+08
⁸⁰ Zr	1.00E+00 1.01E+00	1.00E+00 1.01E+00	1.55E+00 3.03E+00	1.55E+00 3.30E+00	1.67E+01 8.58E+03	7.46E+01 5.23E+08
⁸¹ Zr	4.00E+00 4.26E+00	1.00E+00 1.00E+00	8.19E+00 1.61E+01	1.01E+00 1.24E+00	8.10E+01 1.34E+05	1.55E+02 7.31E+08
⁸² Nb	1.00E+00 2.13E+00	1.00E+00 1.25E+00	3.36E+00 5.36E+00	2.89E+00 7.25E+00	1.09E+02 3.08E+05	5.56E+02 6.99E+08
⁸³ Nb	6.00E+00 6.82E+00	1.00E+00 1.07E+00	1.22E+01 2.04E+01	1.91E+00 3.26E+00	8.68E+01 1.33E+05	6.91E+01 4.74E+08
⁸³ Mo	1.00E+00 1.38E+00	1.00E+00 1.03E+00	2.21E+00 2.94E+00	1.21E+00 1.72E+00	4.03E+01 1.26E+05	1.25E+02 4.40E+08
⁸⁴ Mo	1.00E+00 1.00E+00	1.00E+00 1.00E+00	1.16E+00 2.02E+00	1.00E+00 1.02E+00	1.65E+01 8.68E+03	2.78E+02 3.64E+09
⁸⁶ Tc	1.00E+00 1.08E+00	1.00E+00 1.33E+00	1.49E+00 2.58E+00	3.69E+00 1.08E+01	1.52E+01 1.36E+04	1.04E+03 1.95E+09
⁸⁷ Tc	1.00E+01 1.01E+01	1.00E+00 1.00E+00	1.05E+01 1.16E+01	1.08E+00 1.65E+00	2.13E+01 4.73E+03	2.45E+02 1.68E+09

TABLE IV. Comparison of calculated ECC for different pairing gaps at stellar temperature of 5.8 GK.

Nuclei	Pairing gap	w(MeV) = 2	w(MeV) = 3	w(MeV) = 5	w(MeV) = 10	w(MeV) = 15	w(MeV) = 20	w(MeV) = 25	w(MeV) = 30
⁴⁵ Sc	Scheme-I	1.05E-49	1.50E-48	1.70E-47	3.77E-45	1.93E-43	2.61E-42	1.84E-41	8.80E-41
	Scheme-II	6.33E-50	8.39E-49	7.68E-48	3.18E-45	1.60E-43	2.12E-42	1.48E-41	7.02E-41
⁵¹ V	Scheme-I	5.27E-50	1.04E-48	3.05E-47	5.21E-45	1.43E-43	1.54E-42	9.75E-42	4.37E-41
	Scheme-II	4.37E-50	8.74E-49	2.75E-47	5.13E-45	1.41E-43	1.52E-42	9.54E-42	4.26E-41
⁵⁴ Fe	Scheme-I	3.52E-49	6.74E-48	1.92E-46	3.55E-44	1.03E-42	1.14E-41	7.27E-41	3.28E-40
	Scheme-II	3.71E-49	7.12E-48	2.00E-46	3.52E-44	1.01E-42	1.12E-41	7.15E-41	3.23E-40
⁵⁵ Fe	Scheme-I	4.23E-49	7.34E-48	1.29E-46	6.05E-45	2.22E-43	3.19E-42	2.37E-41	1.18E-40
	Scheme-II	3.58E-49	6.10E-48	1.03E-46	5.60E-45	2.28E-43	3.25E-42	2.40E-41	1.18E-40
⁵⁶ Fe	Scheme-I	1.68E-49	4.51E-48	2.12E-46	4.42E-44	1.09E-42	1.07E-41	6.37E-41	2.73E-40
	Scheme-II	1.56E-49	4.35E-48	2.14E-46	4.62E-44	1.14E-42	1.12E-41	6.67E-41	2.86E-40
⁵⁶ Mn	Scheme-I	2.82E-50	4.27E-49	6.39E-48	1.42E-45	6.10E-44	7.87E-43	5.43E-42	2.56E-41
	Scheme-II	2.06E-50	2.96E-49	5.26E-48	2.11E-45	8.34E-44	1.02E-42	6.86E-42	3.18E-41
⁵⁸ Mn	Scheme-I	7.38E-51	1.83E-49	1.38E-47	5.61E-45	1.70E-43	1.85E-42	1.16E-41	5.13E-41
	Scheme-II	2.92E-51	9.64E-50	1.06E-47	4.70E-45	1.42E-43	1.54E-42	9.61E-42	4.25E-41
⁵⁸ Fe	Scheme-I	3.11E-49	8.52E-48	3.71E-46	6.03E-44	1.27E-42	1.15E-41	6.42E-41	2.64E-40
	Scheme-II	3.01E-49	8.27E-48	3.60E-46	5.86E-44	1.24E-42	1.11E-41	6.22E-41	2.56E-40
⁵⁹ Co	Scheme-I	6.92E-50	1.22E-48	2.54E-47	3.12E-45	1.02E-43	1.23E-42	8.34E-42	3.90E-41
	Scheme-II	4.66E-50	7.91E-49	1.62E-47	2.75E-45	9.66E-44	1.17E-42	7.89E-42	3.67E-41

TABLE V. Comparison of EC rates for selected nuclei at three temperatures (5, 25 and 30 GK) at three densities (10^1g/cm^3 , 10^4g/cm^3 and 10^8g/cm^3) with respect to different pairing gaps.

Nuclei	T (GK)	10^1g/cm^3		10^4g/cm^3		10^8g/cm^3	
		Scheme-I	Scheme-II	Scheme-I	Scheme-II	Scheme-I	Scheme-II
⁴⁵ Sc	5	-4.243	-4.132	-4.241	-4.131	-2.375	-2.257
	25	1.643	1.653	1.643	1.653	1.703	1.713
	30	2.268	2.256	2.268	2.257	2.303	2.292
⁵¹ V	5	-5.111	-5.103	-5.110	-5.102	-2.974	-2.963
	25	1.873	1.886	1.873	1.887	1.934	1.947
	30	2.531	2.538	2.531	2.539	2.566	2.574
⁵⁴ Fe	5	-3.400	-3.432	-3.399	-3.431	-1.275	-1.308
	25	2.059	2.054	2.059	2.055	2.118	2.114
	30	2.516	2.511	2.516	2.512	2.55	2.546
⁵⁵ Fe	5	-2.627	-2.638	-2.626	-2.637	-0.730	-0.743
	25	2.305	2.358	2.306	2.359	2.366	2.419
	30	2.935	2.983	2.935	2.983	2.970	3.018
⁵⁶ Fe	5	-5.784	-5.768	-5.782	-5.767	-3.703	-3.694
	25	1.718	1.742	1.719	1.742	1.779	1.802
	30	2.249	2.277	2.250	2.277	2.284	2.312
⁵⁶ Mn	5	-6.102	-5.585	-6.101	-5.584	-3.901	-3.400
	25	2.080	2.392	2.081	2.393	2.141	2.453
	30	2.766	3.037	2.766	3.038	2.801	3.073
⁵⁸ Mn	5	-7.217	-7.197	-7.216	-7.195	-5.007	-4.988
	25	2.137	2.230	2.138	2.230	2.198	2.290
	30	2.823	2.918	2.823	2.919	2.858	2.954
⁵⁸ Fe	5	-7.424	-7.426	-7.423	-7.424	-5.242	-5.245
	25	1.432	1.455	1.432	1.455	1.492	1.515
	30	2.009	2.031	2.009	2.031	2.044	2.066
⁵⁹ Co	5	-5.187	-5.260	-5.186	-5.258	-3.066	-3.146
	25	1.755	1.774	1.755	1.775	1.816	1.835
	30	2.453	2.471	2.453	2.472	2.488	2.507